J Bionic Eng 18 (2021) 346–360
DOI: https://doi.org/10.1007/s42235-021-0031-1

Journal of Bionic Engineering
http://www.springer.com/journal/42235

3D Printed Multi-material Medical Phantoms for Needle-tissue Interaction Modelling of Heterogeneous Structures

Jun Yin[1,2], Manqi Li[1,2], Guangli Dai[3], Hongzhao Zhou[1*], Liang Ma[1], Yixiong Zheng[4*]

1. *The State Key Laboratory of Fluid Power and Mechatronic Systems*, *School of Mechanical Engineering*, *Zhejiang University*, *Hangzhou* 310028, *China*
2. *Key Laboratory of 3D Printing Process and Equipment of Zhejiang Province*, *School of Mechanical Engineering*, *Zhejiang University*, *Hangzhou* 310028, *China*
3. *Department of Medical Engineering*, *Ningbo First Hospital*, *Ningbo* 315010, *China*
4. *Department of Surgery*, *the Second Affiliated Hospital*, *School of Medicine*, *Zhejiang University*, *Hangzhou* 310009, *China*

Abstract

The fabrication of multi-material medical phantoms with both patient-specificity and realistic mechanical properties is of great importance for the development of surgical planning and medical training. In this work, a 3D multi-material printing system for medical phantom manufacturing was developed. Rigid and elastomeric materials are firstly combined in such application for an accurate tactile feedback. The phantom is designed with multiple layers, where silicone ink, Thermoplastic Polyurethane (TPU), and Acrylonitrile Butadiene Styrene (ABS) were chosen as printing materials for skin, soft tissue, and bone, respectively. Then, the printed phantoms were utilized for the investigation of needle-phantom interaction by needle insertion experiments. The mechanical needle-phantom interaction was characterized by skin-soft tissue interfacial puncture force, puncture depth, and number of insertion force peaks. The experiments demonstrated that the manufacturing conditions, *i.e*. the silicone grease ratio, interfacial thickness and the infill rate, played effective roles in regulating mechanical needle-phantom interaction. Moreover, the influences of material properties, including interfacial thickness and ultimate stress, on needle-phantom interaction were studied by finite element simulation. Also, a patient-specific forearm phantom was printed, where the anatomical features were acquired from Computed Tomography (CT) data. This study provided a potential manufacturing method for multi-material medical phantoms with tunable mechanical properties and offered guidelines for better phantom design.

Keywords: 3D printing, biomimetic, multi-material medical phantom, needle-phantom interaction, Finite Element Analysis (FEA)

1 Introduction

In recent decades, medical phantoms play an important role in medical resident training and surgical planning. For example, in the field of surgical planning, traditional medical imaging techniques, *i.e*. Computed Tomography (CT), Magnetic Resonance Imaging (MRI), are main tools for diagnosis and preoperative planning, but these approaches fail to provide precise information of orientation and dimension, leading to misinterpretation and on-site improvisation[1]. Therefore, medical phantoms, working as tangible objects, benefit surgeons by providing spatial sense and tactile feedback, and help decreasing medical error during surgery. Although, biological tissues, *i.e*. cadavers and animal models, have been widely used in medical training, these materials still have several disadvantages. First, material properties of tissues *in vitro* are quite different from *in vivo*[2], and material properties dramatically change with time[3]. Second, biological tissues degrade too fast with very limited durability. Third, cadavers are not always feasible due to practical issues and bioethical considerations. To overcome these disadvantages, haptic robotic medical training platforms have been developed for better understanding of clinical procedures and decreasing medical errors in healthcare area[4,5]. However, the sophisticated haptic feedback models are needed when various surgical tools and tool properties, such as needle bevel, length and thickness, are taken into account[5]. Also, the success rate of injections depended on variables associated with patient conditions including obesity, site of injection, and subcutaneous fat depth[6].

***Corresponding author:** Hongzhao Zhou, Yixiong Zheng
E-mail: hz_zhou@zju.edu.cn, 2100011@zju.edu.cn

Thus, the research on developing medical phantoms with accurate and adaptive anatomical features is required, and it should be associated with a proper replicate of the native tissues' mechanical properties.

Generally, materials used for phantom manufacturing are rigid-plastic and elastomeric materials. Rigid-plastic materials, *i.e*. Acrylonitrile Butadiene Styrene (ABS), Polylactic Acid (PLA) and VeroTM family resins, are very stiff (Young's modulus ~ 1 GPa), which are used to mimic tissues of higher impact strength and less deformation. While, elastomeric materials, *i.e*. Thermoplastic Polyurethane (TPU), silicone, and TangoTM family resins, are more flexible (Young's modulus ~ 10 MPa – 100 MPa), allowing surgeons to perform different rehearsal operations on them, such as cutting and suturing. Using different materials, various medical phantoms have been fabricated. For example, Biglino *et al*.[7] used TangoPlus resin to fabricate arterial flow phantoms by PolyJet technique, in order to mimic arterial distensibility. Qiu *et al*.[8] 3D printed a prostate model with silicone-based material, showing similar mechanical properties in static and dynamic compression to prostate tissues. Jiang *et al*.[9] fabricated Polyvinylalcohol (PVA) phantoms to investigate the needle insertion of prostate tissues. Despite various applications of medical phantoms, phantoms manufactured in previous studies were based on a single material, which is difficult to mimic surgical operations involving injecting or cutting through multi-layer tissues. Thus, how to fabricate multi-material phantoms to mimic the nature of multi-layer tissues and to serve as surgical aids is still a problem in medical training and preoperative planning. In previous studies[10,11], phantoms with multiple layers have been produced by conventional means of moulding and casting. Li *et al*.[10] fabricated multi-layer PVA phantoms by varying the PVA concentration in each layer, aiming to study the insertion force vibration. Moreover, Pepley *et al*.[11] adjusted the ratio of PVC/softener/mineral oil in moulded multi-layer phantoms to regulate the needle insertion force. However, these moulded multi-layer phantoms are in bulk structure and lacking in anatomical features, and patient-specific phantoms with heterogeneous anatomical structures are too complicated to be fabricated by moulding and casting. The recently developed multi-nozzle 3D printing technology is found to be a promising approach to effectively fabricate patient-specific multi-layer phantoms based on patient information obtained from 3D imaging technology. Zein *et al*.[12] manufactured the artificial livers with TangoTM and VeroTM family resins using Polyjet technology, and demonstrated the identical anatomical and geometrical landmarks in phantoms and native livers. Also, Wake *et al*.[13] used HeartPrint Flex and VeroTM family resins to fabricate kidney phantoms with renal tumour by Polyjet technology, showing spatial relationship of tumour to the renal artery, vein, and collecting system.

For current medical training studies, the function of medical phantoms is not only required to mimic the anatomical features of tissues[13–15], but also to represent the mechanical properties of tissues[16,17]. Forte *et al*.[18] developed a composite hydrogel to mimic the mechanical response of brain tissue under loading. Leibinger *et al*.[15] developed several phantom materials to match the physical properties of brain tissues, including stiffness, fracture behaviour, and transparency. Due to the wide use of medical needles in medical training, *i.e*. suturing[19], epidural anaesthetic procedure[20], and percutaneous procedures[21], the mechanical interaction between needle and phantom is of great importance to effective medical training. de Jong *et al*.[22] used PVA as a liver tissue mimicking material to study the image-guided needle interventions. Wang *et al*.[23] demonstrated the feasibility of using silicone-based material to mimic soft tissues for needle insertion phantoms with realistic haptic feedback. However, the needle-phantom interaction in multi-material phantoms has not been systematically studied yet. Besides experimental studies, Finite Element Analysis (FEA) was utilized for needle insertion modelling. For example, Oldfield *et al*.[24] used a FEA with cohesive elements to model the needle insertion into soft tissue phantoms, enabling direct comparison of numerical and experimental force–displacement plots and energy distributions. However, more sophisticated finite element models have to be established to identify the crack creation, relaxation, cutting and full penetration during needle insertion into phantoms.

In this study, a 3D printing method is presented to fabricate a heterogeneous phantom, which is used to mimic the needle-tissue interaction. Rigid and elasto-

meric materials are firstly combined together using a 3D printing method, for a needle-phantom with adjustable tactile feedback. FEA analyses and bench-top tests were carried out to systemically investigate the influences of material and manufacturing parameters on the mechanical properties of the printed model. This study provides a method for manufacturing multi-material phantom with tunable mechanical properties and helps understand the mechanism of needle-phantom interaction, leading to facilitate design modifications to the phantom.

The materials and manufacturing method are introduced in section **2**, including a multi-nozzle extrusion-based 3D printing system was utilized to manufacture the multi-material phantoms. Customized silicone ink, TPU, and ABS were chosen as printing materials for skin, soft tissue, and bone layers, respectively. The influences of manufacturing conditions, *i.e.* the silicone grease ratio in silicone ink, skin-soft tissue interfacial thickness, and the infill rate of soft tissue layer, on needle-phantom interaction were systematically investigated by needle insertion experiments. In section **3**, a FEA was performed to investigate the process of needle insertion into multi-material phantom. The numerical results agreed well with experimental needle insertion force-depth curves, which is discussed in section **4**.

2 Materials and methods

2.1 Materials and characterization

ABS filaments with diameter of 1.75 mm (PA-777E, CHIMEI, China) and TPU filaments with diameter of 1.75 mm extruded from TPU granules (TPU365A, Desmopan, Germany) were used for Fused Deposition Modeling (FDM) printing. The customized silicone ink was prepared by adding silicone grease (F-01, RUNSA, China) into silicone sealant with room temperature vulcanization formulation (737, DOWSIL, US). The customized silicone ink was vacuumed before pneumatic dispensing printing.

The mechanical properties of printing materials were characterized by uniaxial tensile tests[25] using a dynamic mechanical analysis instrument (ElectroForce, TA Instruments, US). ABS, TPU and silicone sealant were fabricated as dumbbell specimens by moulding with a length of 25 mm, a width of 4 mm and a thickness of 2 mm. In the uniaxial tensile test, ABS, TPU and silicone sealant samples were stretched at displacement rates of 1 mm·min^{-1}, 450 mm·min^{-1}, 450 mm·min^{-1} respectively, and Young's modulus of samples was calculated as the slope of the linear region in the 0% – 0.1% strain range of the stress-strain curves.

Table 1 Bulk properties of polymer materials ([a] measured by experiments, [b] supplied by the vendors)

	ABS	TPU	Silicone sealant
Young's modulus (MPa)[a]	743.0	6.8	1.1
Ultimate tensile strength (MPa)[a]	32.0	16.0	1.4
Tensile strain[a]	0.29	26.84	12.29
Density (Kg·m^{-3})[b]	1070	1154	1040
Thermal conductivity (W·m^{-1}·k^{-1})[b]	0.1	0.1	/
Specific heat (J·kg^{-1}·K^{-1})[b]	1423.5	1800	/
Decomposition temperature (˚C)[b]	375	280	/

The material properties of bulk TPU, ABS and silicone sealant are listed in Table 1. The Young's modulus of native human bone varies from 0.1 GPa to 30 GPa, which depends on the type and position[26]. Titanium alloy biomimetic parts are commonly used in the load bearing bone reconstruction treatments[27–29]. In this research, as a mimic of hard tissues the artificial bone is used as a support, which does not require a high load bearing property. ABS is therefore selected due to its accessible manufacturing conditions. Compared with the soft materials used on the phantom, ABS is assumed to be rigid in this research.

2.2 Multi-nozzle 3D printing system for phantom fabrication

The schematic of custom-made multi-nozzle 3D printing system was developed as shown in Fig. 1, consisting of a building stage and extrusion nozzles. The extrusion nozzles travel parallel to the *X*-*Y* plane over a building stage, while the building stage lowers along the *z* direction by a predetermined distance after one layer is deposited. The extrusion-based 3D printing system consists of three printing nozzles, two FDM liquefier nozzles to extrude ABS and TPU filaments, respectively, and a pneumatic dispensing nozzle to extrude the customized silicone ink. The manufacturing conditions are listed in Table 2, and the printed phantom specimens were kept in an oven under 80 ˚C for 1 h to accelerate vulcanizing process before further measurements.

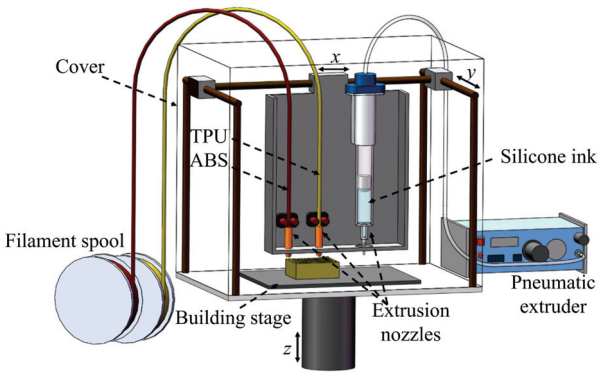

Fig. 1 Schematic of custom-made multi-nozzle 3D printing system.

Table 2 Manufacturing conditions of multi-material phantoms

	TPU	ABS	Silicone ink
Nozzle temperature (°C)	215	210	/
Layer thickness (mm)	0.2	0.2	0.6
Temperature of building stage (°C)	60	60	/
Printing speed ($mm \cdot s^{-1}$)	6	6	5
Extrusion pressure (psi)	/	/	35
Diameter of nozzle (mm)	0.5	0.5	0.838
Silicone grease ratio (R)	/	/	0% – 30%
Interfacial thickness (H) (mm)	0.8 – 2.0	/	/
Infill rate (I)	20% – 50%	/	/

To systematically understand the influence of manufacturing conditions on the needle-phantom interaction, the standard phantom specimens were designed as shown in Fig. 2. The standard phantom specimen consists of a skin layer and a soft tissue layer. The skin layer was set to be 2 mm thick, within the range of human skin thickness (1 mm – 4 mm)[30], while the thickness of soft tissue layer was set as 25.5 mm, which is the average thickness of soft tissue layer of a patient's forearm CT model. The cross section of all specimens is a 20 × 20 mm^2 square. The ABS plates were attached to the bottom and side surfaces to fix the standard phantom specimens, leaving the top surface free for the needle insertion experiment. The mechanical properties of the skin layer were regulated by changing a material parameter, silicone grease ratio (R), which indicates the weight ratio of silicone grease to customized silicone ink. Two other parameters, infill rate (I) and interfacial thickness (H) (Fig. 2), were applied to describe the structural feature of standard phantom specimens. A 45° orientated grid pattern is selected as the infill of the specimen, which offers proper support. The infill layer has different needle force feedback with the interfacial layer, the number of force peaks is a reasonable replicate of the needle-tissue interaction characteristic for human forearm. I refers to the volume ratio of the printed grid lines to the infill area marked by dash line in Fig. 2d, and changing the I only changes the density of grids, rather than the width of the grid lines. H refers to the thickness of skin-soft tissue interface. The interfacial thickness plays an important role in modelling interfacial puncture, and the infill is designed to mimic tissue heterogeneity. Different properties of needle-phantom interaction are achieved by the variation of infill rate, interfacial thickness and silicone grease ratio of standard phantom specimens.

2.3 Needle insertion experiment on phantoms

As shown in Fig. 2a, the needle insertion experiments were performed on phantoms using a dynamic mechanical analysis instrument (ElectroForce, TA Instrument, USA), which included a linear motion stage, a needle and a load sensor. Needles with lancet points were chosen for needle insertion experiments due to their wide use in biopsy, vessel access, brachytherapy and other procedures[31]. The 30-gauge (outer diameter: 0.3 mm) disposal sterile syringe needles with two bevels at tip (SUNGSHIM, Korea) were utilized in the study (Fig. 2b).

The standard phantom specimen (Fig. 2c) was used in needle insertion experiment to investigate the mechanical interaction between needle and phantom. All the insertion tests were carried out at a constant insertion velocity of 0.1 $mm \cdot s^{-1}$, and the insertion depth was 9.5 mm.

2.4 Statistical analysis

More than 5 independent experiments were performed for each condition in this study. All curves of insertion force-depth were filtered by Savizky-Golay filter (polynomial order two). Data were expressed as mean ± standard deviation.

3 FEA of needle insertion into standard phantom specimens

3.1 Constitutive model

In this study, a finite element model is conducted

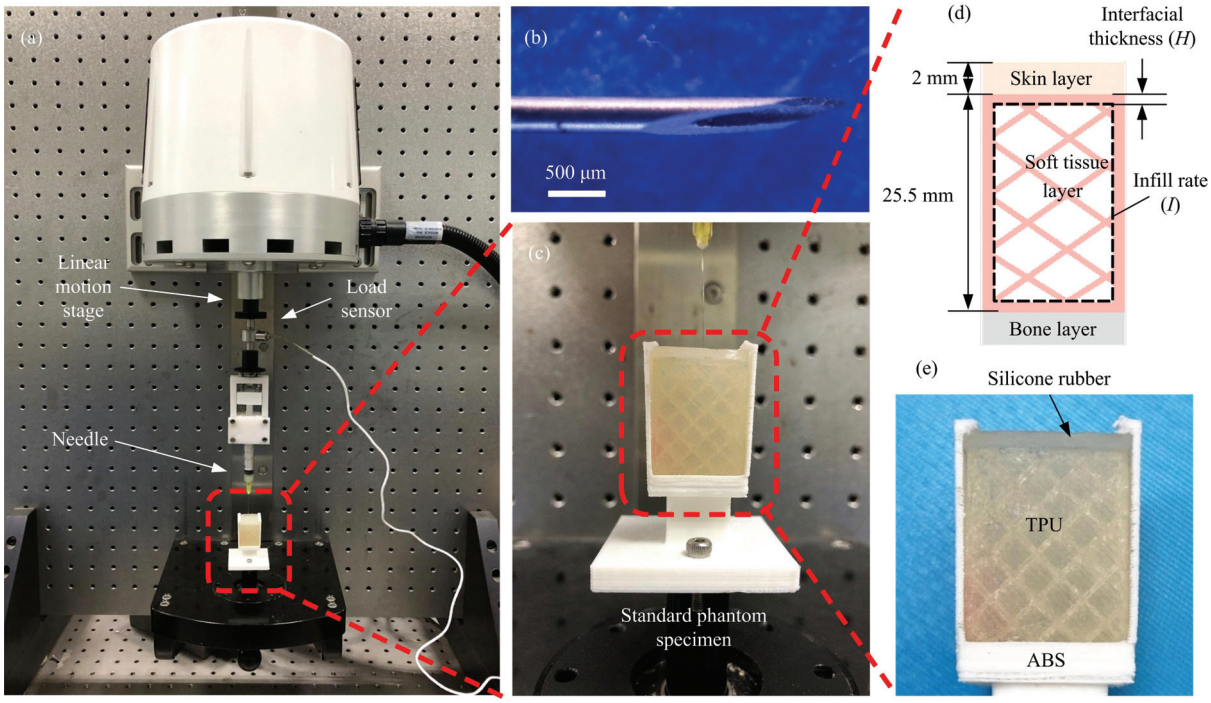

Fig. 2 (a) Experimental setup of needle insertion experiment, (b) needle tip of the 30-gauge syringe needle, (c) standard phantom specimen, (d) schematic of standard phantom specimen, and (e) 3D printed standard phantom specimen.

using the commercial finite element software ABAQUS to understand needle-phantom interaction. The needle was considered as a rigid body[24], where TPU and silicone rubber are assumed to be isotropic, homogeneous and nearly incompressible materials. In order to describe the nonlinear elasticity of these two materials, a hyperelastic constitutive model was implemented, where strain energy density function is in a polynomial form as[32,33]:

$$U = C_{10}(\bar{I}_1 - 3) + C_{01}(\bar{I}_2 - 3) + C_{20}(\bar{I}_1 - 3)^2 + C_{11}(\bar{I}_1 - 3)(\bar{I}_2 - 3) + C_{02}(\bar{I}_2 - 3)^2, \quad (1)$$

where U is the strain energy density function; C_{10}, C_{01}, C_{20}, C_{11} and C_{02} are the material constants, which are fitted *via* mean stress-strain curve using a material evaluation tool provided by ABAQUS; $\bar{I}_1$ and $\bar{I}_2$ are the first and second deviatoric strain invariant. The stress-strain relation can be calculated as[34,35]:

$$\bar{\bar{S}} = \frac{\partial U}{\partial \bar{\bar{E}}}, \quad (2)$$

where $\bar{\bar{S}}$ is the second Piola-Kirchhoff stress tensor and $\bar{\bar{E}}$ is the Green strain tensor.

The phantom material failure model was considered in needle insertion simulation to determine the failure and deletion of phantom element. The criteria for element failure is described as when

$$\|\vec{\sigma}_v\| \geq \|\vec{\sigma}_s\|, \quad (3)$$

in a certain element, the element will be deleted from mesh, where σ_v is the von Mises equivalent stress of element, and σ_s is the ultimate stress of material.

The friction between phantom and needle during needle insertion was described by Coulomb friction model, where friction stress along the needle direction is defined as:

$$\tau = \mu p, \quad (4)$$

where p is the contact pressure and μ is the friction coefficient.

3.2 Determination of material constants

The material constants of the strain energy density function in Eq. (1), C_{10}, C_{01}, C_{20}, C_{11} and C_{02} were determined for TPU and silicone rubber by numerically fitting the experimental results of the uniaxial tensile tests using material evaluation in ABAQUS.

To determine σ_s and μ for TPU and silicone rubber,

the needle insertion experiment was carried out, and the puncture force and puncture depth were recorded. The needle insertion tests were carried out on a TPU sample with 2 mm thickness and a silicone rubber sample with 0.8 mm thickness at a constant insertion velocity of 0.1 mm·s^{-1}, with the insertion depth of 3.5 mm, and the cross sections of both TPU and silicone rubber samples are 20 × 20 mm^2. Also, the finite element modelling was performed, and σ_s and μ were adjusted to numerically fit the experimental data of puncture force and puncture depth.

3.3 Finite element modelling

The numerical model of needle insertion into the standard phantom specimen (as illustrated in Figs. 2d and 2e) was developed to systematically analyse the influence of manufacturing conditions on the needle-phantom interaction. As shown in Fig. 3, the needle model was built based on the geometric information of needles in experiments, while the thickness of skin layer, interface and soft tissue layer of standard phantom model were 2 mm, 0.8 mm and 12.75 mm, respectively. The thickness of infill in soft tissue layer was 0.4 mm. Based on the boundary constraint in needle insertion experiment, the bottom, left and right surfaces of the standard phantom model were fixed, and the axisymmetric boundary condition on *Y*-*Z* plane was set during simulation. Mesh of the area in contact with the needle was refined as shown in the insets in Fig. 3.

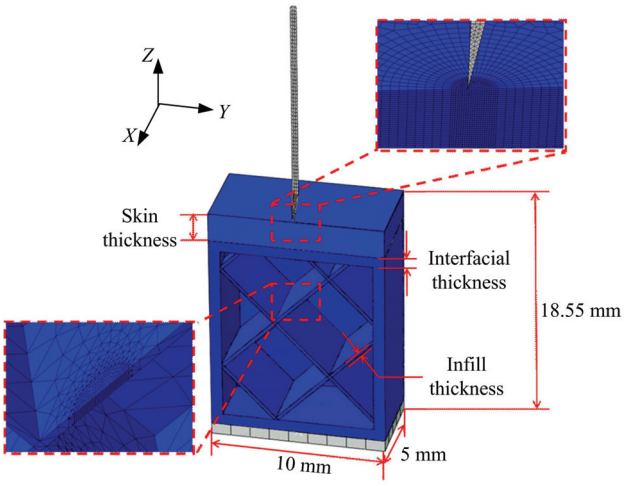

Fig. 3 The finite element model of needle insertion into standard phantom specimen.

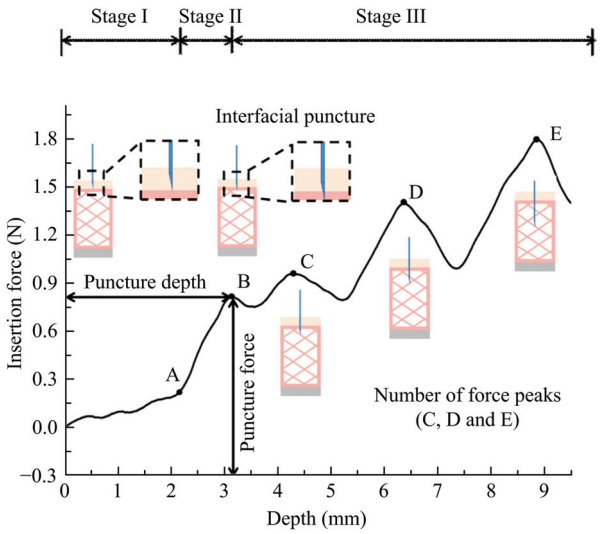

Fig. 4 Representative insertion force-depth curve of the needle insertion into the standard phantom specimen.

4 Results

4.1 Insertion force-depth curves of needle-standard phantom specimen interaction

The needle insertion experiments were performed to characterize the mechanical interaction between needle and phantoms. The representative insertion force-depth curve of a needle insertion into a standard phantom specimen (I = 50%, H = 0.8 mm, R = 0%) is shown in Fig. 4, and the needle insertion process is divided into three stages. The first insertion stage covers the curve from initial position to point A, which corresponds to the needle penetration of skin layer (point A in Fig. 4). In this stage, the insertion force increases when the needle tip contacts the skin layer surface and deforms skin layer, and then the needle tip inserts into the skin layer, until the touching of soft tissue layer. It is noticed that the needle puncturing force at the skin surface cannot be clearly defined in the insertion force-depth curve of the first stage. The second stage of needle insertion is defined from point A to point B, corresponding to penetration of skin-soft tissue interface. In this stage, insertion force rapidly increases when the needle presses and deforms the soft tissue surface. Then, the needle punctures the skin-soft tissue interface, and the insertion force peak is obtained in the insertion force-depth curve (point B in Fig. 4). The third stage covers the curve from point B to the end, which corresponds to the insertion of soft tissue layer. In this stage,

several force peaks appear in the insertion force-depth curve (peaks C, D and E in Fig. 4) due to the process of needle tip contact, deforming and penetrating through the infill of soft tissue layer. Therefore, the parameters of the insertion force-depth curves *i.e.*, puncture force, puncture depth, and number of force peaks are utilized to further characterize the insertion force-depth curves.

4.2 Puncture force and depth on standard phantom specimens

The puncture force occurs when needle tip penetrates through skin-soft tissue interface, which generally measures the minimum force required to insert into soft tissue layer. The influence of manufacturing conditions, *i.e.* *I*, *H* and *R* (Table 2), on puncture force is shown in Figs. 5a – 5c. It can be found that puncture force increases with increasing *I* and *H*, while decreasing *R*. Before skin-soft tissue interfacial puncture, soft tissue layer is compressed by needle pressure, thus the increasing of *I* adds more supports of soft tissue, and the stiffness of soft tissue is enhanced. Also, increasing the *H* leads to a larger compressive modulus of soft tissue. Therefore, the puncture force increases with both *I* and *H* of soft tissue layer. While, the silicone grease enhances the lubricity of skin layer, reducing the friction between the needle shaft and the whole skin layer, thus a smaller puncture force is found when *R* is increased. Based on the results in Figs. 5a – 5c, *H* is the most effective parameter affecting the puncture force, while *R* only slightly adjusts the puncture force.

Figs. 5d – 5f illustrate the influence of *I*, *H* and *R* on puncture depth. Puncture depth is found to increase with *H* and *R*, and decrease with *I*. Obviously, a larger *H* increases the puncture depth by increasing the physical thickness of skin-soft tissue interface. While, influence of *I* and *R* regulate the puncture depth mainly by changing skin-soft tissue interface stiffness. Larger *R* leads to a softer skin layer as well as a more deformable skin-soft tissue interface, thus the puncture depth becomes larger. While, a smaller *I* reduces supports of skin-soft tissue interface during needle insertion. When *R* increases or *I* decreases, the skin-soft tissue interface is easier to deform under the needle pressure, leading to a larger puncture depth. It can be concluded that *H* has a significant effect on puncture depth, while *I* and *R* have the slighter degree of impact on puncture depth.

4.3 Number of insertion force peaks

As shown in Fig. 6, once needle inserts into soft tissue layer, local peaks of insertion force appear in the

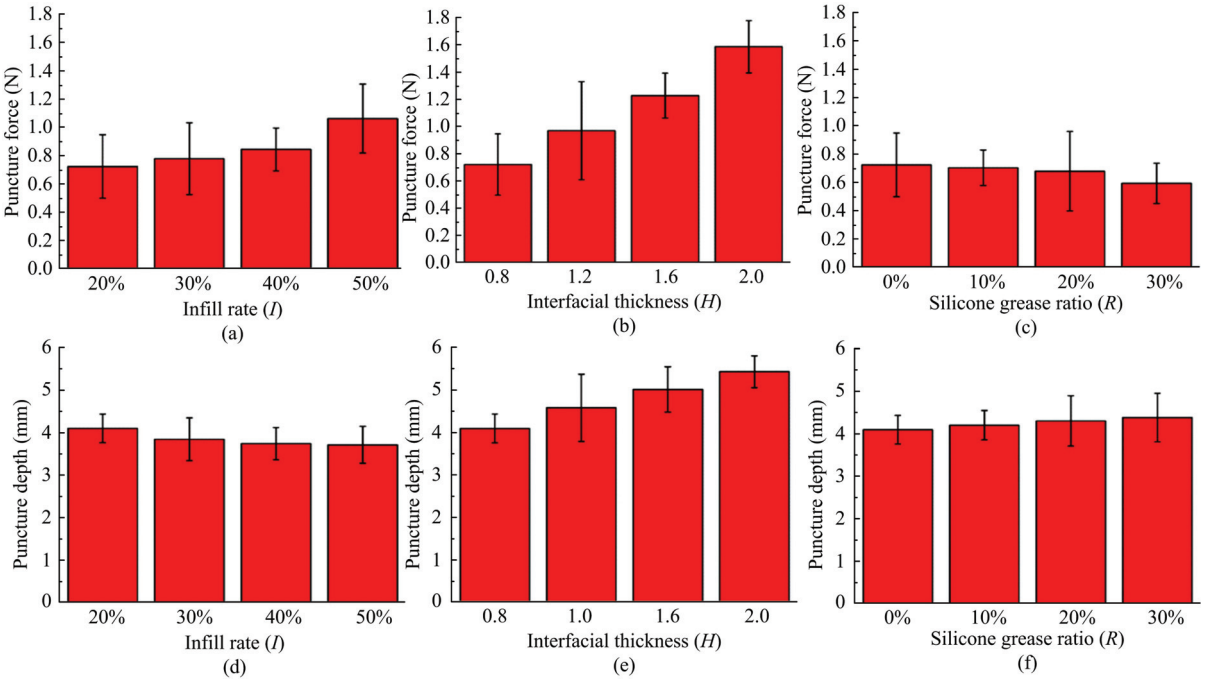

Fig. 5 Average and standard deviation of (a, b, c) puncture force and (d, e, f) puncture depth for needle insertion into standard specimens with different *I*, *H*, *R*.

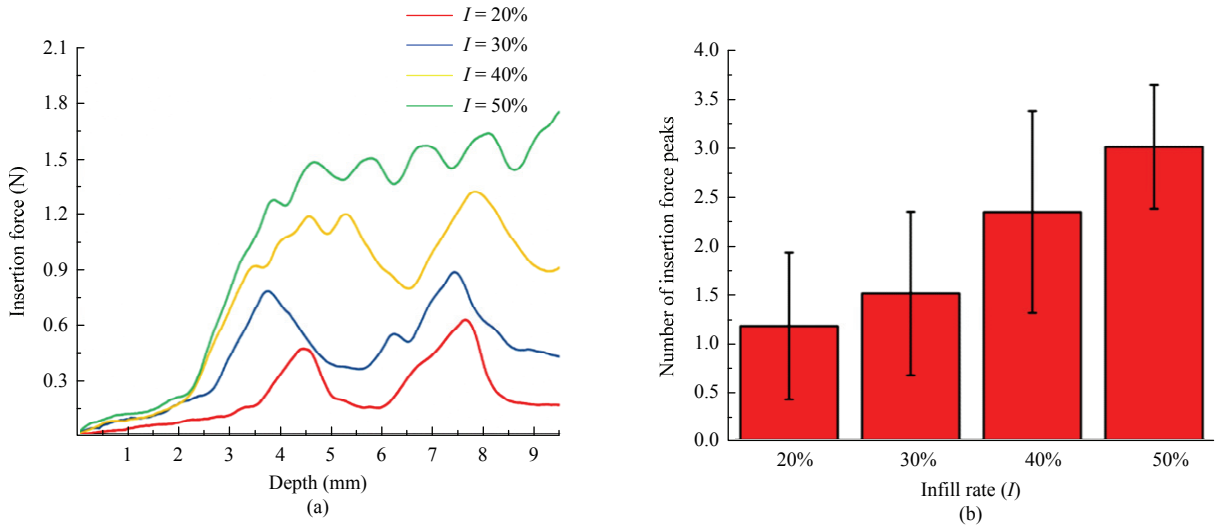

Fig. 6 (a) Representative insertion force-depth curve for needle insertion into standard phantom specimens with different I and (b) number of insertion force peaks for needle insertion into standard phantom specimens with different I.

insertion force-depth curve. Since the local peaks of insertion force occur due to the needle penetration of infills in the soft tissue layer, I significantly influences the number of local peaks of insertion force in the insertion force-depth curve. As shown in Fig. 6, the number of local peaks of insertion force increases when I increases from 20% to 50%. The increase of I leads to a denser infill, so when more infills are punctured during needle insertion, more local peaks of insertion force are shown in the insertion force-depth curve. Therefore, suitable degrees of specimen heterogeneity can be obtained by adjusting I in order to mimic different tissues.

4.4 Numerical simulation of needle insertion into standard phantom specimen

The values of material constants in the numerical model are listed in Table 3. ABS parts are considered as rigid bodies, and their elastic behaviours are neglected. As shown in Figs. 7a and 7b, there are good agreements between numerical fitting strain-stress curves and experimental stress-strain curves, which demonstrates that the values of C_{10}, C_{01}, C_{20}, C_{11}, and C_{02} in the numerical model are appropriate as the material constants of constitutive equations of silicone and TPU. Also, in Figs. 7c and 7d the numerical and experimental results of needle insertion into silicone and TPU materials are very close, so the material constants σ_s and μ in Table 3 are appropriate to describe phantom material failure and friction between needle and phantom.

Table 3 Material constitutive parameters

	TPU	Silicone rubber
C_{10} (MPa)	-5.23×10^{-1}	-4.59×10^{-2}
C_{01} (MPa)	2.16	2.41×10^{-1}
C_{20} (MPa)	2.75×10^{-5}	7.29×10^{-6}
C_{11} (MPa)	7.52×10^{-3}	1.49×10^{-6}
C_{02} (MPa)	1.53×10^{-1}	2.28×10^{-2}
μ	0.2	0.2
σ_s (MPa)	8	2

The representative numerical needle insertion process was shown in Figs. 8a – 8f. Also, numerical and experimental representative insertion force-depth curves of standard phantom specimen (I = 20%, H = 0.8 mm, R = 0%) were shown in Figs. 8g and 8h, respectively. It is noticed that typical insertion stages are observed from numerical results, which show similar trends with experimental results. For instance, in Figs. 8g and 8h points A and B correspond to the needle penetration of skin layer (Fig. 8c) and skin-soft tissue interface (Fig. 8d), respectively. Points C and D refer to force peaks caused by punctures of infills (Figs. 8e and 8f). It can also be seen from insets in Figs. 8d – 8f) that a higher stress always appears in the elements near the needle tip, and the values of von Mises stress are 7.84 MPa, 8 MPa and 6.92 MPa respectively, which are close to TPU ultimate stress 8 MPa. When the failure criteria (Eq. (3)) is satisfied elements are deleted from the mesh, which

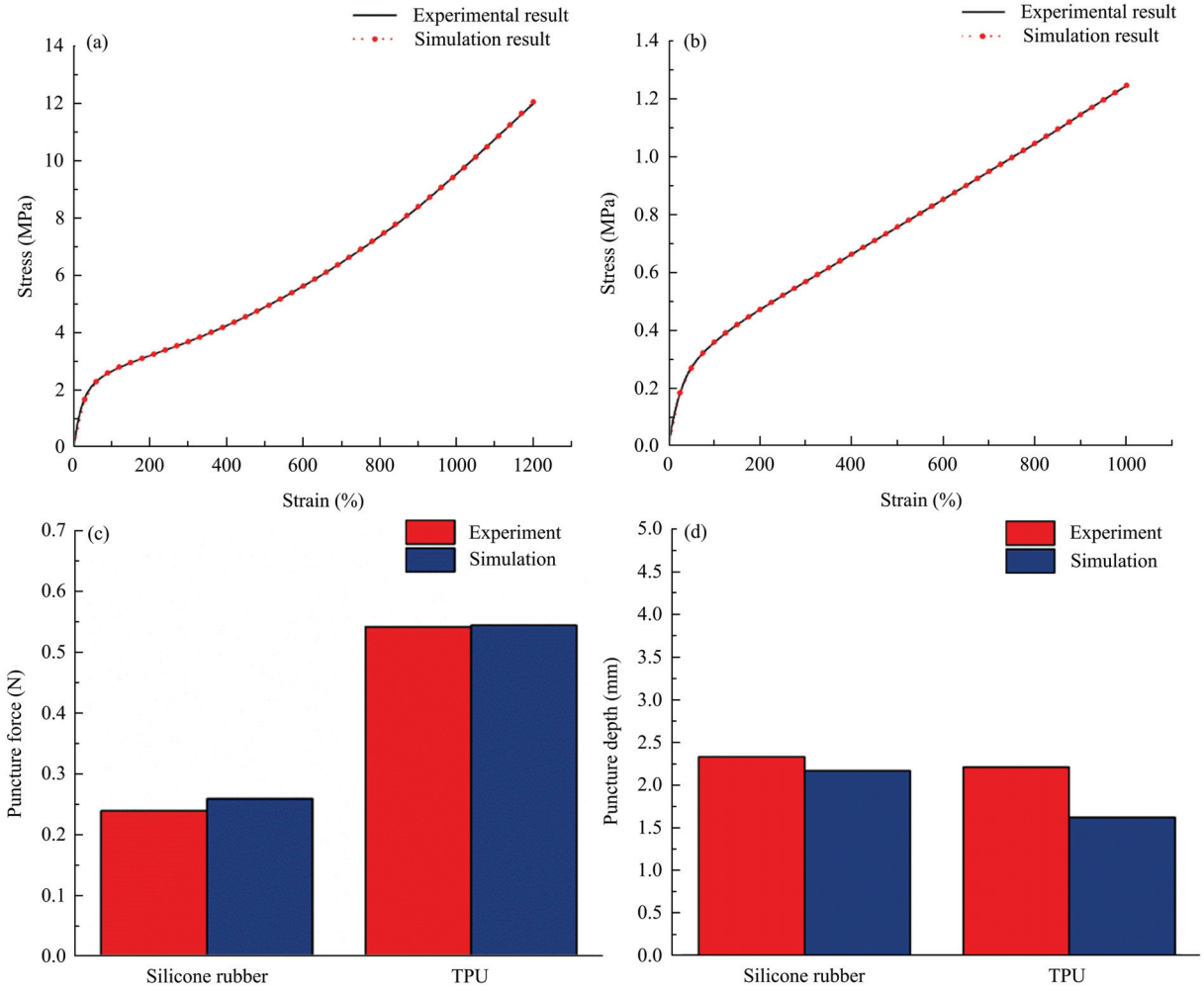

Fig. 7 Numerical and experimental stress-strain fitting curves of (a) silicone and (b) TPU. Numerical and experimental results of (c) puncture depth and (d) puncture force in needle insertion into silicone rubber and TPU.

realizes emergence of crack and needle insertion. Therefore, this simulation model helps understand mechanical needle-phantom interaction.

One goal of this work is to understand the relation between manufacturing conditions and needle-phantom interaction. H is a structural parameter indicating the thickness of skin-soft tissue interface. Figs. 9a and 9b show that both interfacial puncture force and depth increase with H, which has a consistent trend with the experimental results. σ_s is a material parameter measuring the maximum stress that the material can stand during needle insertion process. In order to achieve the heterogeneity of biological tissues, a gridding infill structure was designed inside the soft tissue layer as shown by Fig. 2d. In the numerical simulation of needle insertion, puncture forces and depths when needle penetrates through the skin-soft tissue interface, the first and second gridding infills inside the soft tissue layer were recorded in Figs. 9c and 9d. It is also found that both the puncture force and puncture depth increase with σ_s. Since some material parameters, *i.e.* σ_s, are not easy to regulate in experiments, needle insertion modelling is an ideal complement to experimental observation and offers guidelines for phantom design.

5 Discussion

Since biological tissues are generally mechanically heterogeneous, the insertion force does not proportionally increase with the insertion depth during needle insertion. For instance, liver, functioning to filter and process blood, contains a substantial number of arteries and veins and is considered as heterogeneous[36,37]. To

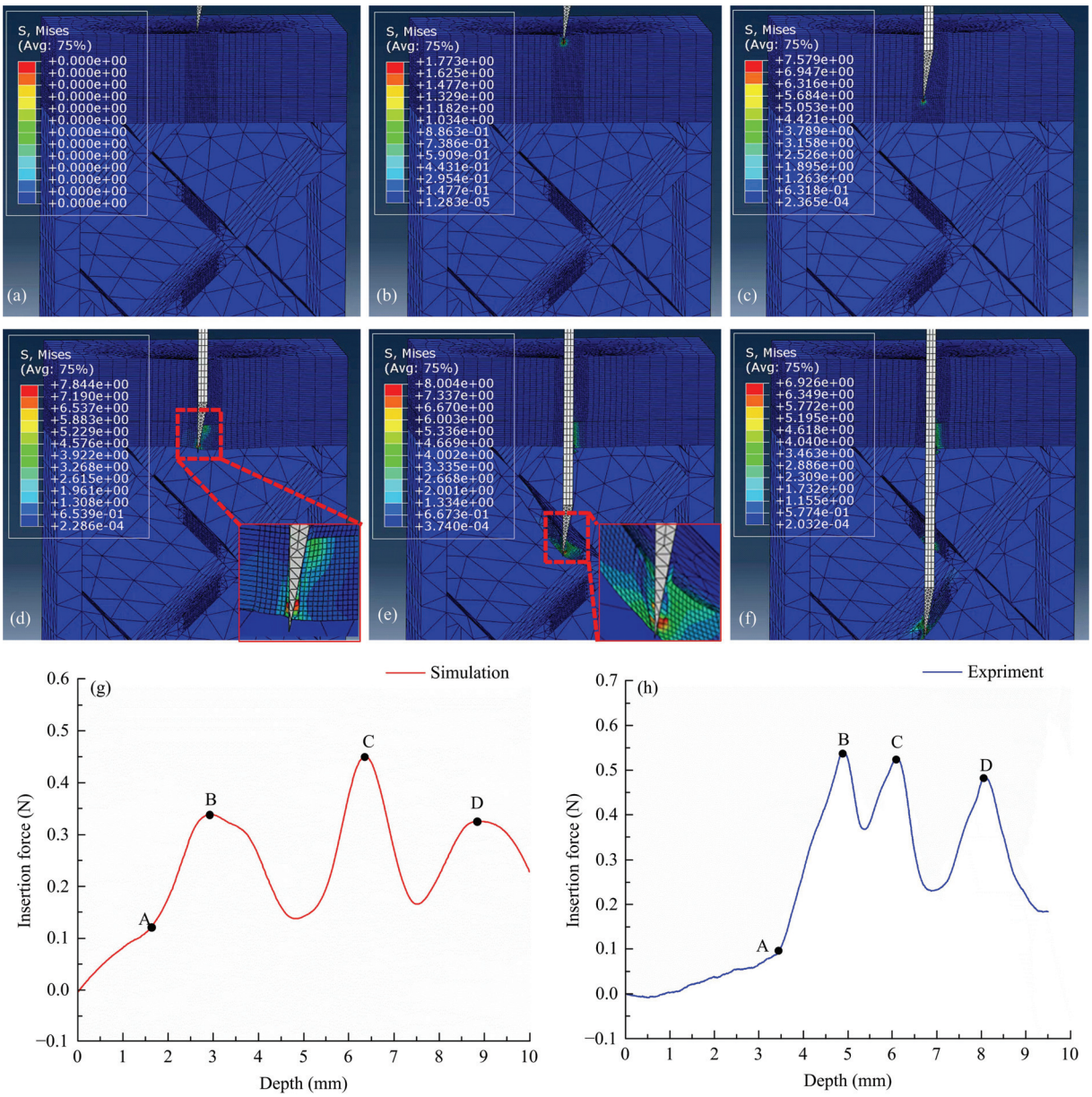

Fig. 8 Insertion process of needle insertion simulation into standard phantom specimen ($I = 20\%$, $H = 0.8$ mm, $R = 0\%$). (a) Initial position; (b) insertion into skin layer; (c) penetration of skin layer; (d) puncture of skin-soft tissue interface; (e) puncture of the first infill; (f) puncture of the second infill; (g) numerical and (h) experimental insertion force-depth curve of the needle insertion into standard phantom specimen.

provide a more realistic needle-phantom interaction in medical training, in this study, we developed a multi-material 3D printing technique for manufacturing phantoms with multiple layers using customized silicone ink, TPU and ABS. The Young's modulus of silicone sealant (1.11 MPa), TPU (6.80 MPa) were found to be in the same level of the Young's modulus of skin (0.1 MPa – 2 MPa[38]) and muscle (0.42 MPa – 12.03 MPa[39]). Moreover, except for multi-layer structure, infill structural design was used to adjust the mechanical heterogeneity of printed phantoms. Hence, the penetration through multiple layers and interior structures leads to force peaks in the insertion force-depth curve during needle insertion. The number of insertion force peaks reflects the degree of heterogeneity of a phantom during the needle-phantom interaction. In addition, the puncture of phantom infills induces sudden jumps in the insertion force-depth curve, so the infill structural design provides

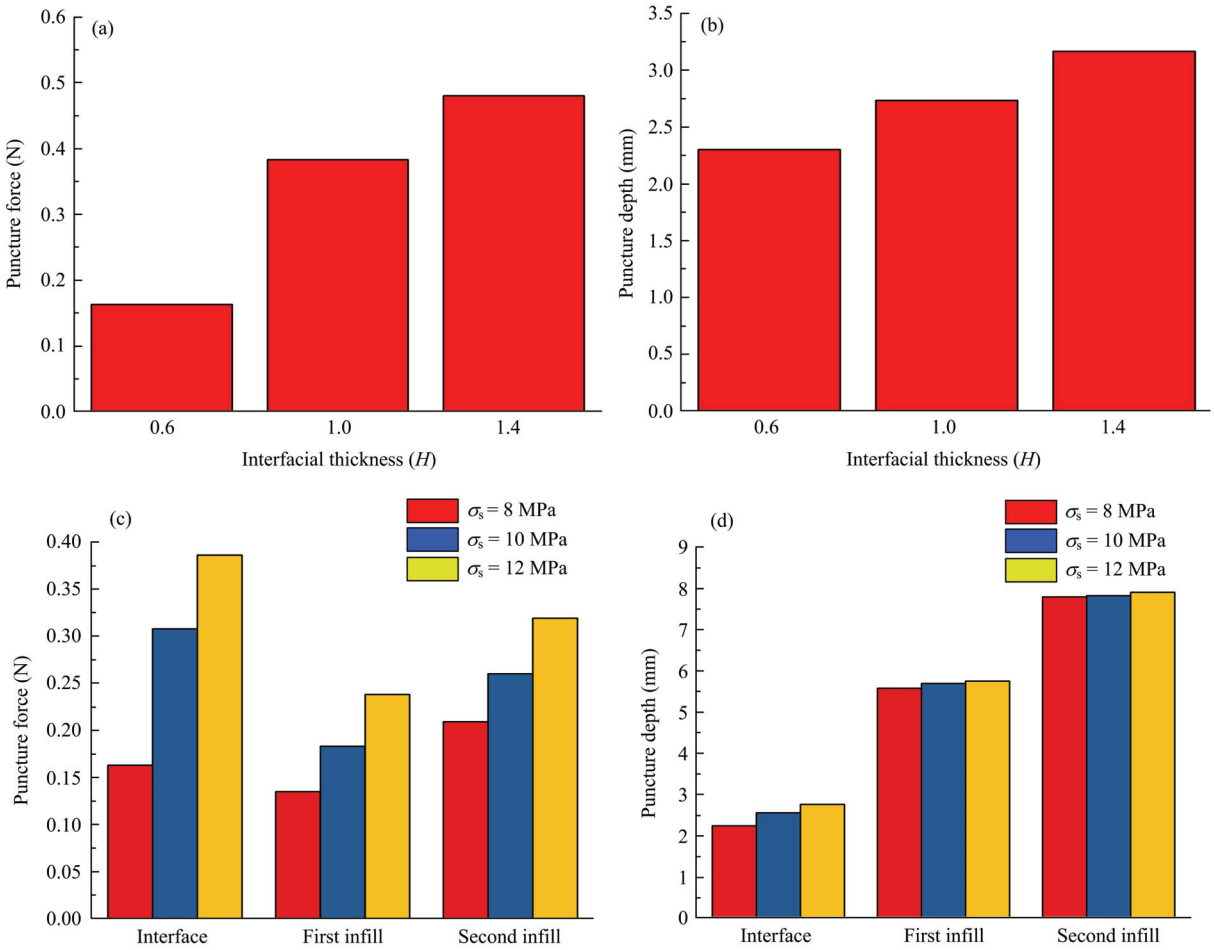

Fig. 9 (a, c) Puncture force and (b, d) puncture depth of needle insertion simulation into standard specimen with various H and σ_s.

a more flexible strategy to manufacture phantoms with multiple degrees of heterogeneity. Since the degree of heterogeneity significantly varies for different organs/tissues, the infill structural design and subsequent multi-material 3D printing method can be utilized to obtain a better mimicry of biological tissues.

Furthermore, the printed multi-layer medical phantoms were applied in the study of needle-phantom interaction. Here, the needle-phantom interaction was characterized by skin-soft tissue interfacial puncture force and puncture depth, and the number of insertion force peaks. In previous studies, mechanical properties of tissue-mimicking phantoms are mainly adjusted by changing the material components[17,23,40] and number of freeze-thaw cycles during PVA phantom preparation[22] to match the mechanical properties of biological tissues. However, printing conditions were rarely reported to tune the needle-phantom interaction properties of tissue mimicking phantoms. This is the first time, to our knowledge that the needle-phantom interaction is adjusted by 3D printing conditions, *i.e.* H and I of phantoms, and the printing material component, *i.e.* the silicone grease ratio in R, to achieve tuneable mechanical properties.

Besides mechanically heterogeneity and tuneable mechanical properties, patient specificity is also of great importance for phantom serving as a kind of surgical planning aid. With the help of medical imaging systems, the proposed method has a great potential of manufacturing the patient specified phantoms. Therefore, a phantom with detailed forearm anatomical features was printed as demonstration in Fig. 10. The model was reconstructed from a patient's CT data with the resolution of 1 mm (Fig. 10a). To mimic the heterogeneity of human forearm, *i.e.*, epidermis, dermis, subcutaneous fat, muscles and bones, the patient-specific phantom was

divided into three layers (Fig. 10b): skin layer (including epidermis and dermis), soft tissue layer (including subcutaneous fat and muscle) and bone layer. Here, the customized silicone ink, TPU and ABS were utilized to print the skin, soft tissue and bone layers, respectively. Since the thickness of human epidermis and dermis are 0.02 mm – 0.15 mm and 1 mm – 4 mm, respectively[36], the total thickness of skin layer was set as 2 mm, and the skin layer was bonded to soft tissue layer by silicone sealant. Bone layer was constructed following the method introduced in Ref. [41]. Therefore, phantom with patient specificity can be 3D printed by the manufacturing method, and this patient specific forearm phantom is able to provide anatomical information of orientation and dimension, which better assists surgical planning and medical training. For the development of more sophisticated phantom, mimicking the realistic material-tissue interaction at cellular level remains to be explored[42–44]. Further investigations are needed to evaluate the similarity between the printed phantom and the original tissues, including *in vivo* tests and big data analysis, which would help optimizing the filament and the printing parameter selection.

6 Conclusion

In this work, medical phantoms with multi-layer structure and tuneable mechanical properties were fabricated by a multi-material 3D printing system. The needle-phantom interaction was studied by needle insertion experiment and finite element simulation, and mechanical properties of phantom insertion can be altered in a controlled manner by varying manufacturing conditions including structural parameters and material parameters. Larger silicone grease ration in skin layer leads to smaller puncture force and larger puncture depth. Increasing interfacial thickness significantly increases puncture force and puncture depth. Larger infill rate in soft tissue layer leads to larger puncture force and number of force peaks while smaller puncture depth. Moreover, with the anatomical information from CT image, patient-specific phantoms were also fabricated. This study is helpful for the development of realistic needle insertion phantoms, which can be further used for clinical training and surgical planning.

In addition to these achievements, more efforts need

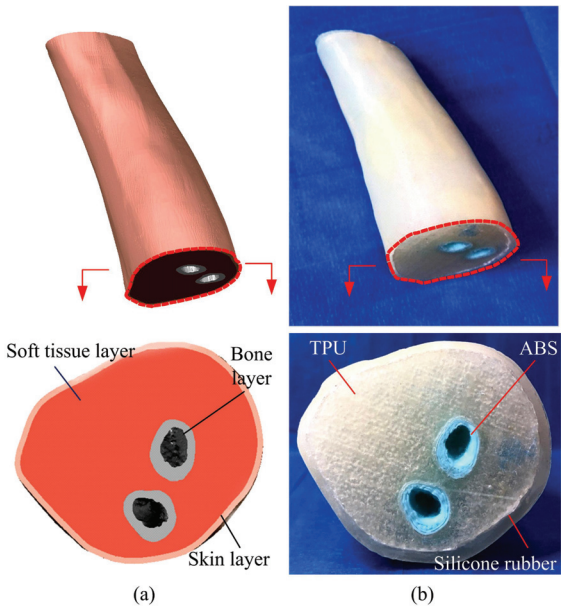

Fig. 10 (a) 3D forearm model reconstructed from CT image and (b) 3D printed patient-specific forearm phantom.

to be done on the development of patient specified medical phantom with integrated functionality. Soft electronic sensors, as developed previously[45,46], will be embedded in phantoms to record the space- and time-varying stress and deformation during phantom performance, which significantly broadens the applicability of phantom in surgical planning and medical training. *In vivo* experiments needs to be done to collect the patient specified data, as a reference for the altering of the filament concentration and printing parameters. Moreover, this study only focused on the needle-phantom interaction, but more physical properties of medical phantoms, *i.e.* radiological fidelity, thermal distribution after ablation procedure, have to be developed.

Acknowledgment

This study was partially supported by the National Key Research and Development Program of China (Grant No. 2018YFA0703000), the National Natural Science Foundation of China (Grant No. 52075482) the Key Research and Development Program of Zhejiang Province (Grant No. 2017C01063) and the National Natural Science Foundation of China (Grant No. 51875518).

References

[1] Mottl-Link S, Hubler M, Kuhne T, Rietdorf U, Krueger J J, Schnackenburg B, De Simone R, Berger F, Juraszek A, Meinzer H P. Physical models aiding in complex congenital heart surgery. *The Annals of Thoracic Surgery*, 2008, **86**, 273–277.

[2] Kobayashi Y, Onishi A, Hoshi T, Kawamura K, Hashizume M, Fujie M G. Development and validation of a viscoelastic and nonlinear liver model for needle insertion. *International Journal of Computer Assisted Radiology and Surgery*, 2009, **4**, 53–63.

[3] Bin Choy Y, Hong C B, Tungjitkusolmun S, Tsai J Z, Haernmerich D, Vorperian V R, Webster J G. Mechanical compliance of the endocardium. *Journal of Biomechanics*, 2002, **35**, 1671–1676.

[4] Gonenc B, Gurocak H. Virtual needle insertion with haptic feedback using a hybrid actuator with DC servomotor and MR-brake with Hall-effect sensor. *Mechatronics*, 2012, **22**, 1161–1176.

[5] Corrêa C G, Nunes F L S, Ranzini E, Nakamura R, Tori R. Haptic interaction for needle insertion training in medical applications: The state-of-the-art. *Medical Engineering & Physics*, 2019, **63**, 6–25.

[6] Soliman E, Ranjan S, Xu T, Gee C, Harker A, Barrera A, Geddes J. A narrative review of the success of intramuscular gluteal injections and its impact in psychiatry. *Bio-Design and Manufacturing*, 2018, **1**, 161–170.

[7] Biglino G, Verschueren P, Zegels R, Taylor A M, Schievano S. Rapid prototyping compliant arterial phantoms for in-vitro studies and device testing. *Journal of Cardiovascular Magnetic Resonance*, 2013, **15**, 1–7.

[8] Qiu K Y, Zhao Z C, Haghiashtiani G, Guo S Z, He M Y, Su R T, Zhu Z J, Bhuiyan D B, Murugan P, Meng F B, Park S H, Chu C C, Ogle B M, Saltzman D A, Konety B R, Sweet R M, McAlpine M C. 3D printed organ models with physical properties of tissue and integrated sensors. *Advanced Materials Technologies*, 2018, **3**, 1700235.

[9] Jiang S, Liu S, Feng, W H. PVA hydrogel properties for biomedical application. Journal of the Mechanical Behavior of Biomedical Materials, 2011; 4: 1228-1233.

[10] Li Q, Gao D D. Research on the stability of needle insertion Force. *Wearable Sensors and Robots*, 2017, **399**, 283–299.

[11] Pepley D F, Sonntag C C, Prabhu R S, Yovanoff M A, Han D C, Miller S R, Moore J Z. Building ultrasound phantoms with modified polyvinyl chloride: A comparison of needle insertion forces and sonographic appearance with commercial and traditional simulation materials. *Simulation in Healthcare*, 2018, **13**, 149–153.

[12] Zein N N, Hanouneh IA, Bishop P D, Samaan M, Eghtesad B, Quintini C, Miller C, Yerian L, Klatte R. Three-dimensional print of a liver for preoperative planning in living donor liver transplantation. *Liver Transplantation*, 2013, **19**, 1304–1310.

[13] Wake N, Chandarana H, Huang W C, Taneja S S, Rosenkrantz A B. Application of anatomically accurate, patient-specific 3D printed models from MRI data in urological oncology. *Clinical Radiology*, 2016, **71**, 610–114.

[14] Farooqi K M, Lengua C G, Weinberg A D, Nielsen J C, Sanz J. Blood pool segmentation results in superior virtual cardiac models than myocardial segmentation for 3D printing. *Pediatric Cardiology*, 2016, **37**, 1028–1036.

[15] Anderson J R, Thompson W L, Alkattan A K, Diaz O, Klucznik R, Zhang Y J, Britz G W, Grossman R G, Karmonik C. Three-dimensional printing of anatomically accurate, patient specific intracranial aneurysm models. *Journal of NeuroInterventional Surgery*, 2016, **8**, 517–520.

[16] Leibinger A, Forte A E, Tan Z C, Oldfield M J, Beyrau F, Dini D, Baena F R Y. Soft tissue phantoms for realistic needle insertion: A comparative study. *Annals of Biomedical Engineering*, 2016, **44**, 2442–2452.

[17] Jiang S, Li P, Yu Y, Liu J, Yang Z Y. Experimental study of needle–tissue interaction forces: Effect of needle geometries, insertion methods and tissue characteristics. *Journal of Biomechanics*, 2014, **47**, 3344–3353.

[18] Forte A E, Galvan S, Manieri F, Baena F R Y, Dini D. A composite hydrogel for brain tissue phantoms. *Materials &*

Design, 2016, **112**, 227–238.

[19] Jackson R C, Çavuşoğlu M C. Modeling of needle-tissue interaction forces during surgical suturing. *IEEE International Conference on Robotics and Automation* (*ICRA*), Saint Paul, MN, USA, 2012, 4675–4680.

[20] Brett P N, Harrison A J, Thomas T A. Schemes for the identification of tissue types and boundaries at the tool point for surgical needles. *IEEE Transactions on Information Technology in Biomedicine*, 2000, **4**, 30–36.

[21] Abolhassani N, Patel R, Moallem M. Needle insertion into soft tissue: A survey. *Medical Engineering & Physics*, 2007, **29**, 413–431.

[22] de Jong T L, Pluymen L H, van Gerwen D J, Kleinrensink G J, Dankelman J, van den Dobbelsteen J J. PVA matches human liver in needle-tissue interaction. *Journal of the Mechanical Behavior of Biomedical Materials*, 2017, **69**, 223–228.

[23] Wang Y, Tai B L, Yu H W, Shih A J. Silicone-based tissue-mimicking phantom for needle insertion simulation. *Journal of Medical Devices*, 2014, **8**, 021001.

[24] Oldfield M, Dini D, Giordano G, Baena F R Y. Detailed finite element modelling of deep needle insertions into a soft tissue phantom using a cohesive approach. *Computer Methods in Biomechanics and Biomedical Engineering*, 2013, **16**, 530–543.

[25] Yin J, Lu C H, Fu J Z, Huang Y, Zheng Y X. Interfacial bonding during multi-material fused deposition modeling (FDM) process due to inter-molecular diffusion. *Materials & Design*, 2018, **150**, 104–112.

[26] Rho J Y, Ashman R B, Turner C H. Young's modulus of trabecular and cortical bone material: Ultrasonic and microtensile measurements. *Journal of Biomechanics*, 1993, **26**, 111–119.

[27] Zhang B Q, Pei X, Zhou C C, Fan Y J, Jiang Q, Ronca A, D'Amora U, Chen Y, Li H Y, Sun Y, Zhang X D. The biomimetic design and 3D printing of customized mechanical properties porous Ti_6Al_4V scaffold for load-bearing bone reconstruction. *Materials & Design*, 2018, **152**, 30–39.

[28] Zhao L, Pei X, Jiang L H, Hu C, Sun J X, Xing F, Zhou C C, Fan Y, Zhang X D. Bionic design and 3D printing of porous titanium alloy scaffolds for bone tissue repair. *Composites Part B*: *Engineering*, 2019, **162**, 154–161.

[29] Pei X, Wu L N, Zhou C C, Fan H Y, Gou M L, Li Z Y, Zhang B Q, Lei H Y, Sun H, Liang J, Jiang Q, Fan Y J, Zhang X D. 3D printed titanium scaffolds with homogeneous diamond-like structures mimicking that of the osteocyte microenvironment and its bone regeneration study. *Biofabrication*, 2021, **13**, 015008.

[30] Dabrowska A K, Rotaru G M, Derler S, Spano F, Camenzind M, Annaheim S, Stampfli R, Schmid M, Rossi R M. Materials used to simulate physical properties of human skin. *Skin Research and Technology*, 2016, **22**, 3–14.

[31] Wang Y, Chen R K, Tai B L, McLaughlin P W, Shih A J. Optimal needle design for minimal insertion force and bevel length. *Medical Engineering & Physics*, 2014, **36**, 1093–1100.

[32] Marckmann G, Verron E. Comparison of hyperelastic models for rubber-like materials. *Rubber Chemistry and Technology*, 2006, **79**, 835–858.

[33] Yin J, Zhang D M, Xiang Y, Wei P, Yang Z Y, Wang Z H, Fu J Z. The influence of cross-sectional morphology on the compressive resistance of polymeric nerve conduits. *Polymer*, 2018, **148**, 93–100.

[34] Yin J, Zhang Z Y. The influence of thyroarytenoid and cricothyroid muscle activation on vocal fold stiffness and eigenfrequencies. *Journal of the Acoustical Society of America*, 2013, **133**, 2972–2983.

[35] Zhang D M, Suo H R, Qian J, Yin J, Fu J Z, Huang Y. Physical understanding of axonal growth patterns on grooved substrates: Groove ridge crossing versus longitudinal alignment. *Bio-Design and Manufacturing*, 2020, **3**, 348–360.

[36] Okamura A M, Simone C, O'Leary M D. Force modeling for needle insertion into soft tissue. *IEEE Transactions on Biomedical Engineering*, 2004, **51**, 1706–1716.

[37] Misra S, Reed K B, Douglas A S, Ramesh K T, Okamura A M. Needle-tissue interaction forces for bevel-tip steerable needles. 2*nd IEEE RAS & EMBS International Conference on Biomedical Robotics and Biomechatronics*, Scottsdale, AZ, USA, 2008, 224–231.

[38] Miller K. Biomechanics of soft tissues. *Medical Science Monitor*, 2000, **6**, 158–167.

[39] Qiang B, Hu H W, Wen J M, Yu Z Y, Zhang S, Jiang Y F, Sun W D. A preliminary determination of foot-related tissue elastic modulus. *Chinese Journal of Tissue Engineering Research*, 2015, **19**, 1919–1923.

[40] Tan Z, Dini D, Baena F R Y, Forte A E. Composite hydrogel: A high fidelity soft tissue mimic for surgery. *Materials & Design*, 2018, **160**, 886–894.

[41] Dong X P, Zhang Y W, Pei Y J, Wang Z, Zhang X X, Yu X L, Ai Z Z, Mei Y X, Li J N. Three-dimensional printing for the accurate orthopedics: Clinical cases analysis. *Bio-Design and Manufacturing*, 2020, **3**,122–132.

[42] Liu H P, Fang C, Gong Z, Chang R C C, Qian J, Gao H J, Lin

Y. Fundamental characteristics of neuron adhesion revealed by forced peeling and time-dependent healing. *Biophysical Journal*, 2020, **118**, 1811–1819.

[43] Dong L Q, Gong J X, Wang Y Z, He J X, You D Q, Zhou Y, Li Q, Liu Y, Cheng K, Qian J, Weng W J, Wang H M, Yu M F. Chiral geometry regulates stem cell fate and activity. *Biomaterials*, 2019, **222**, 119456.

[44] Gong B, Lin J, Wei X, Qian J, Lin Y. Cross-linked biopolymer networks with active motors: Mechanical response and intra-network transport. *Journal of the Mechanics and Physics of Solids*, 2019, **127**, 80–93.

[45] Zhu F, Zheng S Y, Lin J, Wu Z L, Yin J, Qian J, Zheng Q. Integrated multifunctional flexible electronics based on tough supramolecular hydrogels with patterned silver nanowires. *Journal of Materials Chemistry C*, 2020, **8**, 7688–7697.

[46] Zhu F, Lin J, Wu Z L, Qu S, Yin J, Qian J, Zheng Q. Tough and conductive hybrid hydrogels enabling facile patterning. *ACS Applied Materials & Interfaces*, 2018, **10**, 13685–13692.